THE IMPACT OF ROTOR ANGLE OF ATTACK
ON BVI TRAJECTORIES AND ROTOR LOADING CHARACTERISTICS

BY

BEREND G. VAN DER WALL

INSTITUTE OF FLIGHT MECHANICS, DLR BRAUNSCHWEIG
LILIENTHALPLATZ 7, D-38108 BRAUNSCHWEIG, GERMANY

TWENTIETH EUROPEAN ROTORCRAFT FORUM
OCTOBER 4 - 7, 1994 AMSTERDAM

THE IMPACT OF ROTOR ANGLE OF ATTACK
ON BVI TRAJECTORIES AND ROTOR LOADING CHARACTERISTICS

BY

BEREND G. VAN DER WALL

INSTITUTE OF FLIGHT MECHANICS, DLR BRAUNSCHWEIG

LILIENTHALPLATZ 7, D-38108 BRAUNSCHWEIG, GERMANY

Abstract

This paper investigates the effect of rotor shaft angle of attack, varying from $-13.11° \leq \alpha_S \leq +10.14°$, on BVI characteristics, rotor loading and blade motion at constant advance ratio of $\mu = 0.15$ and a constant thrust coefficient of $C_T/\sigma = 0.058$. A 40% Mach scaled BO105 hingeless model rotor has been equipped with a total of 124 absolute pressure transducers in the range of $r/R = 0.6...0.99$ and 32 strain gages (from $r/R = 0.14...0.81$) on one blade. Tests were done in December 1992 in the German-Dutch wind tunnel (DNW) within the European community research program HELINOISE [1] and the DLR program CPROT [2]. With a microphone rig 1.5 radii below the rotor disk, the noise emission of the rotor was recorded. The rotor was trimmed to zero hub moments in pitch and roll direction. Table 1 gives a list of the rotor conditions used for analyses in this paper. These wind tunnel test cases are representing a $2to$ BO105 in different flight path configurations (12° climb to 11° descent) at a flight speed of 64 knots.

Flight path	$\alpha_S/°$	μ	C_T/σ	M_H	P/kW	$N_{max}/\%$	$GF_{4,acc}/\%$
12° climb	-13.11	.148	.05894	.645	51.7	78.1	74.4
6° climb	-7.06	.150	.05816	.644	39.7	82.6	100.0
level flight	-.95	.151	.05790	.644	28.2	87.7	77.4
6° descent	5.05	.149	.05816	.644	17.0	100.0	48.1
11° descent	10.14	.148	.05959	.642	8.0	95.6	39.8

Table 1: Test cases with BVI

The analyses of the leading edge pressure signals in the range of $r/R = 0.6, ..., 0.99$ gives information of where BVI exits and how strong it is. In combination with varying shaft angle of attack, some significant changes of the BVI loacations in the rotor disk can be observed. That is, with increasing α_S the BVI locations move aft by up to about 20% of the radius in some regions. The aerodynamic lift distribution is found to be the origin of this behavior, since with increasing α_S the tip region between $\psi = 145°$ and $\psi = 200°$ becomes unloaded. Thus, the radial gradient in bound circulation becomes small at the tip while it is large more inboard. As a consequence, the tip vortex will not form at the tip, but more inboard (that is downstream in this azimuth range) and thus BVI will happen more downstream, assuming a constant vortex convection velocity in all of these cases. Rotor simulation codes have to model these changes of tip vortex positions appropriately when it comes up to prediction of rotor noise or vibration.

The maximum noise level was found in the 6° descent flight case, where a lot of close and parallel BVI is present in the rotor disk on the advancing and retreating side. At climb or larger descent rates the maximum noise is less since the blade-vortex miss-distances become larger where parallel interaction exists. This reduces the high frequency content of leading edge pressure, known to be the dominant source for BVI noise.

Vibration levels, based on the $4/rev$ components of accelerometers in $x-$, $y-$ and $z-$direction close to the hub in the nonrotating system, are found to be maximum at 6° climb condition. Vibration is due to higher harmonic blade motion, excited by low frequency airloads in the frequency range of $3 - 5/rev$ in the rotating frame. Origin of these airloads are the low frequency components of the rotor wake. The analyses of blade aerodynamic loading at radial stations of $r/R = 0.75$, 0.87 and 0.97 in combination with the blade deflections, calculated from strain gage data, gives some insight into the mechanism.

Due to the reproduction technique, the originally colored graphs on Fig. 2 and Fig. 5 are printed only in black/white[1].

---

[1] The colored originals are available on request from the author in limited number.

Nomenclature

c	airfoil chord [m]	r, R	radial coordinate, radius [m]
$C_T = T/(\rho \pi R^2 V_t^2)$	thrust coefficient	r_c	vortex core radius [m]
EI_f	flap bending stiffness [Nm^2]	t	time [s]
L	section lift [N/m]	T	rotor thrust [N]
$M_{0.25}$	section aerodynamic moment [Nm/m]	$V = V_t(r/R + \mu \sin \psi)$	local velocity [m/s]
M_f	flapwise bending moment [Nm]	$V_t = \Omega R$	tip speed in hover [m/s]
n_b	number of blades	V_T	wind tunnel velocity [m/s]
N_f	number of flap modes	x	chordwise coordinate [m]
P	power [kW]	x_v, y_v	vortex coordinates [m]
P_u, P_l	air pressure on upper and lower side of the airfoil [N/m^2]	z_u, z_l	airfoil vertical coordinate of upper and lower side [m]
q_{fi}	flap mode deflection [m]	z	vertical elastic blade deflection [m]
α_S	shaft angle of attack	$\mu = V_T \cos \alpha_S / V_t$	advance ratio
β	angle between vortex axis and blade leading edge	ρ	air density [kg/m^3]
$\psi = \Omega t, \psi_{BVI}$	rotor azimuth, azimuth of BVI	$\sigma = (n_b c)/(\pi R)$	rotor solidity
		Ω	rotor rotational speed [rad/s]
$\Delta \psi$	peak-to-peak azimuthal distance of a BVI event	ω_{fi}	Eigenfrequency of a flap mode [rad/s]
$\Delta \psi_v$	azimuthal vortex age	ϕ_{fi}	flap mode shape

1 Introduction

The validation of rotor simulation codes requires a detailed knowledge of the aerodynamic force and moment distribution along the rotor blade. In addition, informations about the blade elastic deflections in flap, lead-lag and torsion are needed. To fulfill these needs, four institutes of DLR started a research program CP-ROT (pressure measurement in rotating system) [2]. Details about instrumentation and the high frequency parallel data accquisition system can be found in [3, 4, 5, 6]. First results from the wind tunnel tests in the DNW have been published recently addressing BVI noise [7], as well as BVI and loading characteristics in high speed descent flight at $\mu = 0.314$ and 6° descent at $\mu = 0.15$ [8, 9, 10]. Earlier experiments mainly aimed at BVI noise directivity, generation, and reduction mechnisms, for example [11, 12, 13, 14]. Other experiments tried to isolate the phenomena of BVI via a vortex generator in the windtunnel upstream of the rotor, and the unloaded rotor blade interacting with this externally generated vortex [15, 16]. In this paper, the focus is set on where the tip vortex is created and how this is affecting the BVI trajectories (that are the lines in the rotor disk where BVI occurs) and aerodynamic loading. The latter forces the rotor blade to elastic deformations, that are measured via strain gages. As a result, the deflection can be calculated. With the knowledge of the blade mode shapes in flap, lead-lag and torsion the excitation of each of these modes can be identified and the impact of varying angle of attack on flap motion will be addressed in the last section.

2 BVI trajectories

The methodology to find BVI locations is described in [8]. It is based on the leading edge pressure transducer signals at 3% chord on the upper side of the airfoil at $r/R = 0.6, 0.7, 0.75, 0.8, 0.87, 0.9, 0.94, 0.97$, and 0.99. In this study, the steady part and the first three integer harmonics are subtracted from the raw data to suppress the large low frequency signals that are due to rotor control and wind tunnel velocity. A sample of the result is given for a radial station of $r/R = 0.97$ in Fig. 1. The variation with shaft angle of attack results in a movement of strongest BVI from the leading edge of the disk at $\alpha_S = -13.11^o$ (the rest of the wake is below the rotor) to the rear at $\alpha_S = 10.14^o$, where most of the wake is above the disk. From the time histories, the center between two consecutive peaks is indicating the vortex' passage of the pressure sensor as indicated in Fig. 1 by arrows. The larger the peak-to-peak pressure, the closer the vortex is to the blade. At this radial station, only the vortex of the preceding blade can be identified at $\alpha_S = -13.11^o$ and -7.06^o. A sequence of vortices is present at the other configurations, while the influence of the tip vortex of the preceding blade is vanishing due to its increasing distance to the blade. So far, this behavior can be expected from basic considerations.

Putting the information of these BVI locations of all radial stations together in one plot gives the BVI trajectories in the rotor disk. These are shown in Fig. 2 for all of the five test conditions together with the pressure distribution at 3% chord (upper side), that has been high-pass filtered at $6/rev$ in order to visualize the strongest BVI locations. Beginning in level flight, the rotor hub wake affects the pressure in the rear region from about $\psi = 330°$ to $10°$ with increasing disturbances when increasing the descent rate. Due to this effect, no BVI locations can be identified there. In the front region, especially in descent conditons, the vortices have significant distance to the blade. Additionally, the blade-vortex interaction angle is close to $90°$ (i.e., the vortex axis is about rectangular to the leading edge) and the vortex' influence at a given radial position is present on a wider range of azimuth, both results in low frequency components of the pressure signal. Therefore, the BVI locations in this area were identified from unfiltered pressure time histories.

Assuming the vortex being created at the blade tip, it will be convected downstream by the wind tunnel velocity. Then, the vortex positions in the tip path plane are:

$$
\begin{aligned}
x_v/R &= \cos\psi_v + \mu\Delta\psi_v \\
y_v/R &= \sin\psi_v
\end{aligned}
$$

with $\Delta\psi_v$ being the vortex age in azimuth. With this model, BVI trajectories only depend on μ and only minor differences may be expected in the experimentally evaluated trajectories, since μ variations are small, see Table 1. Plotting all BVI-trajectories and the analytical trajectories from the simple model in one graph, as is done in Fig. 3, shows surprising large differences. In climb configuration, the agreement of the model with the experiment is quite well ($\alpha_S = -13.11°$). In level flight, however, an offset of up to $\Delta X = \Delta x/R \approx 0.13$ can be observed at $Y = y/R = 0.5$ on the advancing side, while the retreating side is almost unaffected. As predicted by theory, three trajectories are present in the front half of the rotor disk. In descent conditions, the BVI trajectories move even more aft, and also on the retreating side of the rotor. The maximum displacement (in comparison to the climb case) is about $\Delta X = \Delta x/R \approx 0.17$ at $Y = y/R = 0.0$ and only two trajectories are found in the first half of the rotor.

A similar behavior was observed in high speed descent flight [8], where a strong negative loading at the blades tip caused two vortices with opposite sense of rotation to be developed; one at the tip and a second one more inboard. Both of the vortices were present in the pressure time histories. In the configurations analysed here, however, no double vortex systems can be found. The pressure time histories only show events that must have been caused by vortices which were developed by a blade with positive lift. A possible explanation might be a larger induced in-plane velocity component in descent flight. In this case, there must be an additional velocity of up to $\Delta\mu = \Delta x/R \approx 0.66\mu$ and it is not clear, where this should come from. Another explanation is a partial unloading of the blades tip in the region between $\psi \approx 110°$ and $250°$. This unloading must be of a special nature, i.e. the gradient to the tip must be very weak while more inboard a strong gradient must be present. Then, the rolled-up vortex will form, where the strongest radial gradient is present, that is inboard with this assumption. The position of this "strongest radial gradient" must be a function of α_S in the test cases under investigation. An answer to this assumption will be given by an analysis of the aerodynamic blade loading in the next section.

The time history of the measured pressure at the leading edge also gives information about the vortex' core radius. Assuming the blade-vortex miss distance to be within or very close to the core radius, r_c, the azimuthal distance $\Delta\psi$ between the two corresponding peaks of a BVI event (see Fig. 1) is a nondimensional measure for the vortex core diameter. This is defined as the geometrical length between the maximum upwash velocity before the vortex' center and the maximum downwash behind it. With β as the angle with which the vortex is interacted ($\beta = 0$ when the blade leading edge and the vortex are parallel), the nondimensional core radius can be evaluated approximately [8]

$$
\frac{r_c}{c} \approx \frac{R}{c}\left(r/R + \mu\sin\psi_{BVI}\right)\frac{\Delta\psi}{2}\cos\beta
$$

From each of the test cases, the location with the largest pressure difference is taken for analyses since this is most likely the position where the vortices are closest to the blade or passing the blade path plane. In climb condition, these positions are within the front half of the rotor while in descent these are found in the rear. Table 2 lists results for a number of BVI events, they are based on the pressure time histories given in Fig. 4. Additionally, the age of the vortex is given by $\Delta\psi_v$.

All of these core radii are in the range of 20% chord, as was found in [8]; the value of $r_c/c = 0.25$ at $11°$ descent is larger, but the vortex is much older in this case. It is also obvious, that the core radii increase with time, i.e. the older the vortex, the larger the core radius. However, for building up a core radius aging function, much more data must be analysed.

Flight path	r/R	μ	$\psi_{BVI}/^\circ$	$\Delta\psi/^\circ$	$\beta/^\circ$	r_c/c	$\Delta\psi_v$
12° climb	0.87	.148	120.0	15.0	85	0.19	80
6° climb	0.97	.150	86.7	5.5	80	0.15	70
level flight	0.99	.151	280.5	5.5	72	0.21	114
6° descent	0.99	.149	295.8	2.2	35	0.22	320
11° descent	0.99	.148	21.4	2.2	40	0.25	670

Table 2: Vortex core radius analysis. $R/c = 16.529$

3 Rotor blade aerodynamic loading

Three sections at $r/R = 0.75, 0.87, 0.97$ were instrumented along chord to obtain the chordwise pressure distribution. The integration of the pressure is done at every data point during the revolution. For the lift, here defined as the aerodynamic force normal to the airfoils' chord, the local pressure is taken as constant along a line between the middle of two neighbouring pairs of sensors. The resulting local force is acting normal to the local surface that is inclined with respect to the airfoils' center line. Thus, with x being here the chordwise coordinate and z_u, z_l the contour coordinate of upper and lower surface, the aerodynamic lift L and moment about quarter chord $M_{0.25}$ are evaluated via the following formula.

$$L = \int_0^c \left[P_l(x) \cos\left(\frac{\partial z_l(x)}{\partial x}\right) - P_u(x) \cos\left(\frac{\partial z_u(x)}{\partial x}\right) \right] dx$$

$$M_{0.25} = \int_0^c \left[P_u(x) \cos\left(\frac{\partial z_u(x)}{\partial x}\right) - P_l(x) \cos\left(\frac{\partial z_l(x)}{\partial x}\right) \right] (0.25c - x)\, dx$$

It is assumed that the tip itself is unloaded, i.e. $L = 0 N/m$ at $r/R = 1$. Then, the lift distribution of the outer 25% of the rotor blade can be calculated and the result is shown in Fig. 5. In climb, there is lift all over the disk. With increasing shaft angle, the tip loading is reduced around the azimuth of $\psi \approx 140^\circ$ ($\alpha_S = -7.06^\circ$). This effect becomes stronger when looking to descent configuration, where the tip around $\psi \approx 170^\circ$ becomes unloaded or even slightly negatively loaded. In these cases, there exists a strong radial gradient in lift not at the tip, but more inboard. This explaines the behavior of the BVI trajectories in Fig. 2 and Fig. 3. The weakly loaded tip in level flight around $\psi \approx 140^\circ$ causes the tip vortex to be created up to about $\Delta r/R = 0.1$ inboard, and this is in the range from $\psi = 105^\circ$ to $\psi = 210^\circ$. In descent, the unloading of the tip is present over an even larger area and the center is shifted towards $\psi = 170^\circ$. By this, the strongest radial gradients in lift are also moved more inboard, and from Fig. 3 the vortex forms at a radial station of about $r/R = 0.8$ at $\psi = 180^\circ$, instead at the tip. This shifts the BVI trajectories downstream and results in two complete vortex encounters in the front of the disk in descent configurations, while in climb and level flight three of them were found there.

The impact of shaft angle of attack on the lift development can be analysed in more detail when applying a fast Fourier tranform to the lift time histories at every radial station. This is done for the first six harmonics in Fig. 6. The steady part of lift continuously is decreasing with larger shaft angle at the outer sections $r/R = 0.97$ and 0.87, while it is little affected at $r/R = 0.75$. Since the total lift is maintained constant for these test cases, the lift loss in the outer sections in descent must be balanced by additional lift in the inner sections. This moves the maximum bound circulation inboard, and with it, the radial gradient of this circulation is either weakened, or, in combination with the harmonic parts, is positioned in some regions at the tip and in others inboard, as has been shown before Fig. 5.

Looking to the lift amplitudes of the first six harmonics in Fig. 6, it is most interesting to focus on the $2/rev$ and $3/rev$ components, that are significantly varying with the flight condition and the radial position. At the outer section $r/R = 0.97$, the $2/rev$ lift is almost zero in climb, but growing with α_S to the largest amplitude of the spectra. The phase is not varying significantly. More inboard at $r/R = 0.87$, the $2/rev$ lift is first decreasing with α_S, has a minimum in level flight, and with a phase shift of 180° is increasing again. The same behavior is observed for the third station $r/R = 0.75$. Thus, in climb the inner part of $2/rev$ lift is in counterphase to the outer station, while in descent all radial sections are in phase with each other.

The $3/rev$ lift components of all three sections are approximately in phase for all the test cases presented here and their amplitude is growing from small values in climb to large values in descent. Since the model rotor has four rotor blades, the 3, 4 and $5/rev$ components of lift are important for vibration in the fixed frame. In all the conditions analysed here the $3/rev$ is the largest one of these. The $4/rev$ lift amplitudes are constant at

$r/R = 0.75$, but undergoing large phase shifts from climb to descent. At $r/R = 0.87$ the amplitudes are growing with α_S, and the phase is shifting significantly. At the outer station, amplitude and phase are about constant.

From basic considerations, the shaft angle is a global parameter of the nonrotating system and shall affect the steady values and the first two harmonics in the rotating system directly. The steady and $1/rev$ are widely cancelled by the rotor trim (adopting the control settings to match the trim condition). The higher harmonics are indirectly affected by the shaft angle, since the global wake position relative to the rotor plane is changing and with it the induced downwash field. Additionally, the BO105 hingeless rotor blades are elastic with the Eigenfrequency of the second flap mode at $\omega_{f2}/\Omega = 2.7$ and the first torsional at $\omega_{\vartheta1}/\Omega = 3.6$. Both of them are close to the $3/rev$ and their motions are also hidden in the lift spectra.

4 Blade motion

The equipment of one blade with 32 strain gages along span allows the measurement of the bending moment distribution in flap, lead-lag and torsion. With the knowledge of the stiffness distribution, the blade elastic deflections can be calculated. For this purpose, the blade is ideally split in sections with constant stiffness, and the bending moment is assumed to vary linearly within this section. Then, the beam bending theory is applied.

$$\frac{d^2 z(r)}{dr^2} = \frac{M_f(r)}{EI_f(r)}$$

For the blade tip, $M_{tip} = 0 Nm$ is assumed and the moment at the root is extrapolated from the first 3 strain gauges: $M_0 = M_1 + \frac{r_0 - r_1}{2}\left[\frac{M_2 - M_1}{r_2 - r_1} + \frac{M_3 - M_1}{r_3 - r_1}\right]$. Then the slope at the end of the section is found by integration as

$$\frac{dz(r)}{dr} = \frac{dz(r)}{dr}\Big|_{j-1} + \frac{M_{f,j-1}}{EI_{f,j}}(r_j - r_{j-1}) + \frac{\partial M_f/\partial r\,|_j}{EI_{f,j}}\frac{(r_j - r_{j-1})^2}{2}$$

and the elastic flap deflection results from a second integration

$$z(r) = z_{j-1} + \frac{dz(r)}{dr}\Big|_{j-1}(r_j - r_{j-1}) + \frac{M_{f,j-1}}{EI_{f,j}}\frac{(r_j - r_{j-1})^2}{2} + \frac{\partial M_f/\partial r\,|_j}{EI_{f,j}}\frac{(r_j - r_{j-1})^3}{6}$$

r_0 is the blade clamp, where geometric boundary conditions are applied. These are zero deflection and zero slope for flap and lead-lag, and zero twist for torsion. The resulting elastic motion can now be Fourier transformed for every radial position. By knowledge of the mode shapes, the deflection of each mode in each harmonic can be identified, since the total deflection is assumed to be the superposition of the deflections of each mode $\phi_{fi}(r)$ (N_f being the number of modes considered):

$$z(r, \psi) = \sum_{i=1}^{N_f} \phi_{fi}(r)\, q_{fi}(\psi)$$

with $q_{fi}(\psi)$ being represented by a Fourier series of M harmonics

$$q_{fi}(\psi) = \frac{a_{i,0}}{2} + \sum_{j=1}^{M}[a_{i,j}\cos(j\psi) + b_{i,j}\sin(j\psi)]$$

By nondimensional mode shapes $\phi_{fi}(r)$ with a tip deflection of unity, the Fourier coefficients directly are the tip deflection of the mode i in the $j - th$ harmonic. This methodology was applied to the first three flap modes, whose mode shapes are shown in Fig. 7, and the result is given in Fig. 8 and Fig. 9, together with the total tip deflection spectrum of the measured data. It is important to note, that the second flap mode has a node at about $r/R = 0.79$ and therefore the lift at $r/R = 0.75$ is not that important for this mode.

The steady value of the measured tip deflection z_{tip}, see Fig. 8, is positive in climb and changes to negative values in descent. This is mainly due to the first mode's steady deflection, q_{f1}. From the steady lift in Fig. 6, it was observed that the lift moves inboard with increasing α_S and thus the aerodynamic moment about the effective flap hinge reduces. Since the centrifugal forces do not change, the coning reduces slightly. The second mode also shows smaller deflection with increasing α_S. This is in agreement with the loading moving inboard, since the lift inside the node tries to bend the tip down while the lift outside bends it up. Only the third mode is almost unaffected by this, since there are two nodes involved, and the various effects cancel each other.

The total tip deflection spectrum z_{tip} in Fig. 9 shows a $1/rev$ amplitude that is unaffected by α_S. This is not surprising because of the trim condition held constant. However, the $2/rev$ and $3/rev$ are changing significantly with the shaft angle. From the table in the abstract Table 1, the largest vibrations in the fixed frame are measured in $6°$ climb, and the behavior of the vibration level widely correlates with the $3/rev$ tip deflection amplitude. In earlier studies with this rotor, the second flap mode was assumed to be the main source for this rotor's vibration [17, 18]. From the total tip deflection in flap direction, however, it is not clear which mode is participating most in the various harmonics. This is clarified by the spectra of each mode in Fig. 9.

It can be seen immediately, that the third flap mode q_{f3} is not participating in the low frequency range. Its Eigenfrequency is close to $5/rev$, where slightly larger amplitudes can be found, but this mode is well damped by aerodynamic forces. The $1/rev$ amplitude of the total deflection is produced for $2/3$ by the first flap mode q_{f1} and for $1/3$ by the second flap mode q_{f2}, both with the same phase. This amplitude represents the tip path plane angle relative to the shaft axis, and from the phase being at $270°$ this means the tip path plane is tilted down to the right by about $0.25°$. It is widely unaffected by the flight condition since the rotor trim is held constant. Surprisingly, the phase of $1/rev$ blade motion is the same as the phase of the lift in the outer sections, see Fig. 6. One would expect a phase delay in flap of about $80°$ of flap motion relative to the lift, because the Eigenfrequency of the first flap mode is slightly larger than the $1/rev$. A closer look to the $1/rev$ phase of lift at $r/R = 0.75$, however, indicates a significant phase shift ahead of the outer sections. It is unknown, how the $1/rev$ lift phases behave even more inboard, but overall they must have the dominant effect for the first flap mode.

The $3/rev$ amplitudes of the second mode are found to be larger than those of the first mode, having a maximum, where vibrations also were found to be largest. From the lift spectra in Fig. 6, all radial sections show up with increasing amplitudes from climb to descent, but the phases remain almost constant. Due to this frequency being far over the its Eigenfrequency, the first mode shows a phase delay of about $180°$ with respect to the lift. Its amplitudes are basically growing with the lift amplitudes. The second flap mode shows different behavior. Although its phase also is about $180°$ past the lift, its amplitudes do not follow the lift amplitudes. The reason must be seen in the mode shape: The node at about $r/R = 0.8$ reduces the effect of lift amplitudes around this node, but the most important effect is at the tip and around $r/R = 0.5$, where this mode has its largest deflections. In case the lift amplitudes grow more around $r/R = 0.5$ than at the tip, and have the same phase, they will balance more and more of the lift at the tip and as a consequence, the second flap mode will remain without deflection in this frequency. This behaviour is found for the second flap mode with increasing shaft angle, however, no loadings could be measured inside of $r/R = 0.75$ with this instrumentation and thus the proof of this thesis has still to be given.

5 Summary

A 40% Mach scaled BO105 hingeless model rotor was equipped with 124 abolute pressure sensors and 32 strain gages, all on one rotor blade. From the pressure time histories along the leading edge, BVI events can be identified. The loading of the outer 25% span can be analysed from chordwise pressure distribution. Blade deflections are evaluated via beam bending theory using the bending moment distribution measured by the strain gages.

At constant advance ratio of $\mu = 0.15$ an constant trim condition the effect of shaft angle of attack on BVI trajectories, rotor loading and blade motion is analysed. It is shown, that due to global changes of the rotor loading the location, where the tip vortex is created, is significantly changing. The tip vortex can be created up to 20% more inboard in descent flight condition due to partial unloading of the blade tip in the front region of the rotor disk. This is visible in the BVI trajectories, leading to large variations in the blade-vortex interaction geometry.

The steady lift distribution is depending on the shaft angle in that way, that the tip region is more and more unloaded while the loading inboard is growing with increasing α_S. A very significant effect is found in the $2/rev$ and $3/rev$ lift components. In $2/rev$, large changes in both amplitude and phase are found differently at each of the sections analysed. In contrast to this, the $3/rev$ lift amplitudes increase with shaft angle at all radial stations and their phase is about the same.

From the bending moment distribution, the total blade flap deflection can be calculated. From this basis, and with the knowledge of the first flap mode shapes, the deflections of each single mode can be identified. The second flap mode shows dominant amplitudes in the $3/rev$, these being even larger than those of the first flap mode, but with the same phase. The dependency of the second flap mode on the shaft angle shows up in the total flap deflection at the tip and also in the vibration. This supports the assumption made in earlier studies, that the second flap mode must be the main source of vibration of this rotor.

References

[1] V. Klöppel, "Helicopter and Tilt-Rotor Aircraft Exterior Noise Research (HELINOISE)," *BRITE/EURAM Aeronautic Days*, 1991

[2] B. Junker "CP-ROT - Ein DLR-Kooperationsprogramm,' *DLR-Nachrichten*, Heft 75, 1994

[3] W.R. Splettstößer, K.J. Schultz, B. Junker, W. Wagner, B. Weitemeier, "The HELINOISE Aeroacoustic Rotor Test in the DNW," *DLR-Mitt. 93-09*, Braunschweig, 1993

[4] B. Gelhaar, K. Alvermann, F. Dzaak, "A Rotor Acoustic Data Acquisition System Based on Transputer and Sigma Delta Converters," *European Test and Telemetering Conference*, Toulouse, France, 1991

[5] B. Gelhaar, K. Alvermann, F. Dzaak, "A Multichannel Data Acquisition System Based on Parallel Processor Architectures," *International Telemetering Conference*, San Diego, CA, USA, 1992

[6] B. Gelhaar, B. Junker, W. Wagner, "DLR - Rotor Teststand Measures Unsteady Rotor Aerodynamic Data," *19th European Rotorcraft Forum*, Como, Italy, 1993

[7] W.R. Splettstößer, G. Niesl, D.G. Papanikas, F. Cenedese, F. Nitti, "Experimental Results of the European Helinoise Aeroacoustik Rotor Test in the DNW," *19th European Rotorcraft Forum*, Como, Italy, 1993

[8] B.G. van der Wall, "- CP-ROT - First Results from Pressure Instrumented BO105 Hingeless Model Rotor Tests," *19th European Rotorcraft Forum*, Como, Italy, 1993

[9] B. van der Wall "Mit CP-ROT am Puls der Rotoren,' *DLR-Nachrichten*, Heft 75, 1994

[10] B. van der Wall "- CP-ROT - Erste Ergebnisse eines Drucksensorbestückten gelenklosen Modellrotors vom Typ BO105,' *DGLR Jahrestagung*, Göttingen, 1993

[11] D.A. Boxwell, F.H. Schmitz, W. Splettstößer, K.J. Schultz, "Model Helicopter Rotor High Speed Impulsive Noise: Measured Acoustic and Blade Pressures," *9th European Rotorcraft Forum*, Stresa, Italy, 1983

[12] Y.H.Yu, A.J. Landgrebe, S.R. Liu, P.F. Lorber, M.J. Pollack, R.M. Martin, D.E. Jordan, "Aerodynamic and Acoustik Test of a United Technologies Model Scale Rotor at DNW," *46th Annual Forum of the American Helicopter Society*, Washington, D.C., 1990

[13] M.K. Lal, S.G. Liou, G.A. Pierce, M.M. Komerath, "Measurements of Unsteady Pressure on a Pitching Rotor Blade," *49th Annual Forum of the American Helicopter Society*, St. Louis, Missouri, 1993

[14] R. Kube, M. Achache, G. Niesl, W.R. Splettstößer, "A Closed Loop Controller for BVI Impulsive Noise Reduction by Higher Harmonic control,' *48th Annual Forum of the American Helicopter Society*, Washington, D.C., 1992

[15] F.X. Caradonna, R.C. Strawn, "An Experimental and Computational Study of Rotor-Vortex Interactions," *14th European Rotorcraft Forum*, Milano, Italy, 1988

[16] M.B. Horner, E. Saliveros, R.A.McD. Galbraith, "An examination of vortex convection effects during blade-vortex interaction," *Zeitschrift für Flugwissenschaften und Weltraumforschung*, Bd. 17, 1993

[17] R. Kube, "New Aspects of Higher Harmonic Control at a Four Bladed Hingeless Model Rotor,' *15th European Rotorcraft Forum*, Amsterdam, The Netherlands, 1989

[18] R. Kube, "Simultaneous Vibration and BVI Noise feedback for Closed Loop Higher Harmonic Control: Influence of Rotor Dynamics on Controller Design,' *19th European Rotorcraft Forum*, Como, Italy, 1993
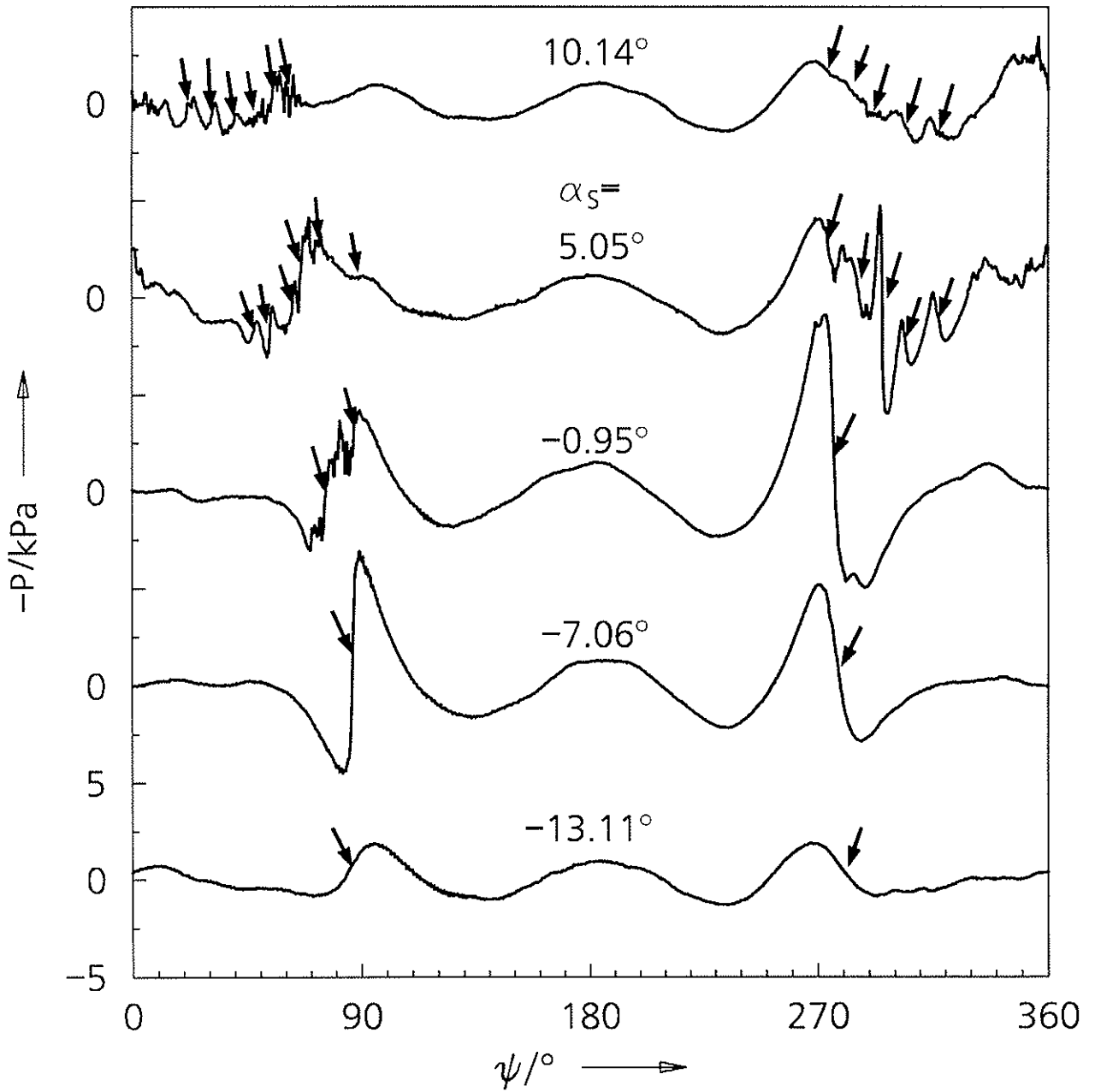
Figure 1: Variation of BVI induced pressure as a function of shaft angle of attack. BVI locations are marked with an arrow.

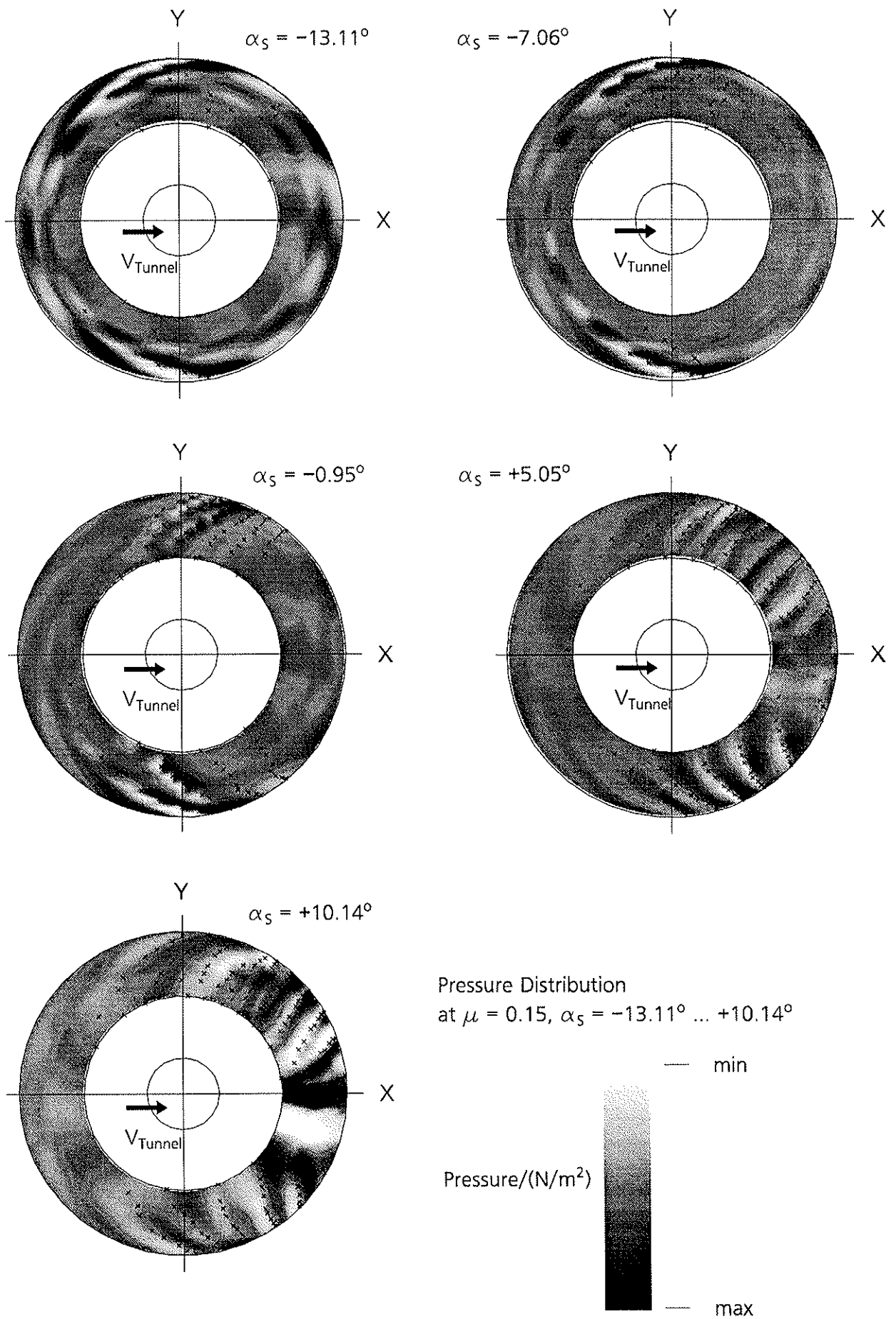Figure 2: Blade pressure (high-pass filtered at 6/*rev*) and BVI trajectories in the rotor disk.

Theory ++++++

Exp., $\alpha_S = -13.11°$ ————

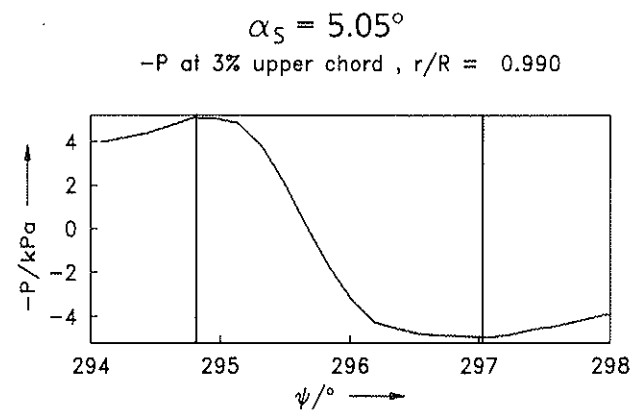Exp., $\alpha_S = -0.95°$ — — —

Exp., $\alpha_S = 10.14°$ — · —

Y

X

V_{Tunnel}
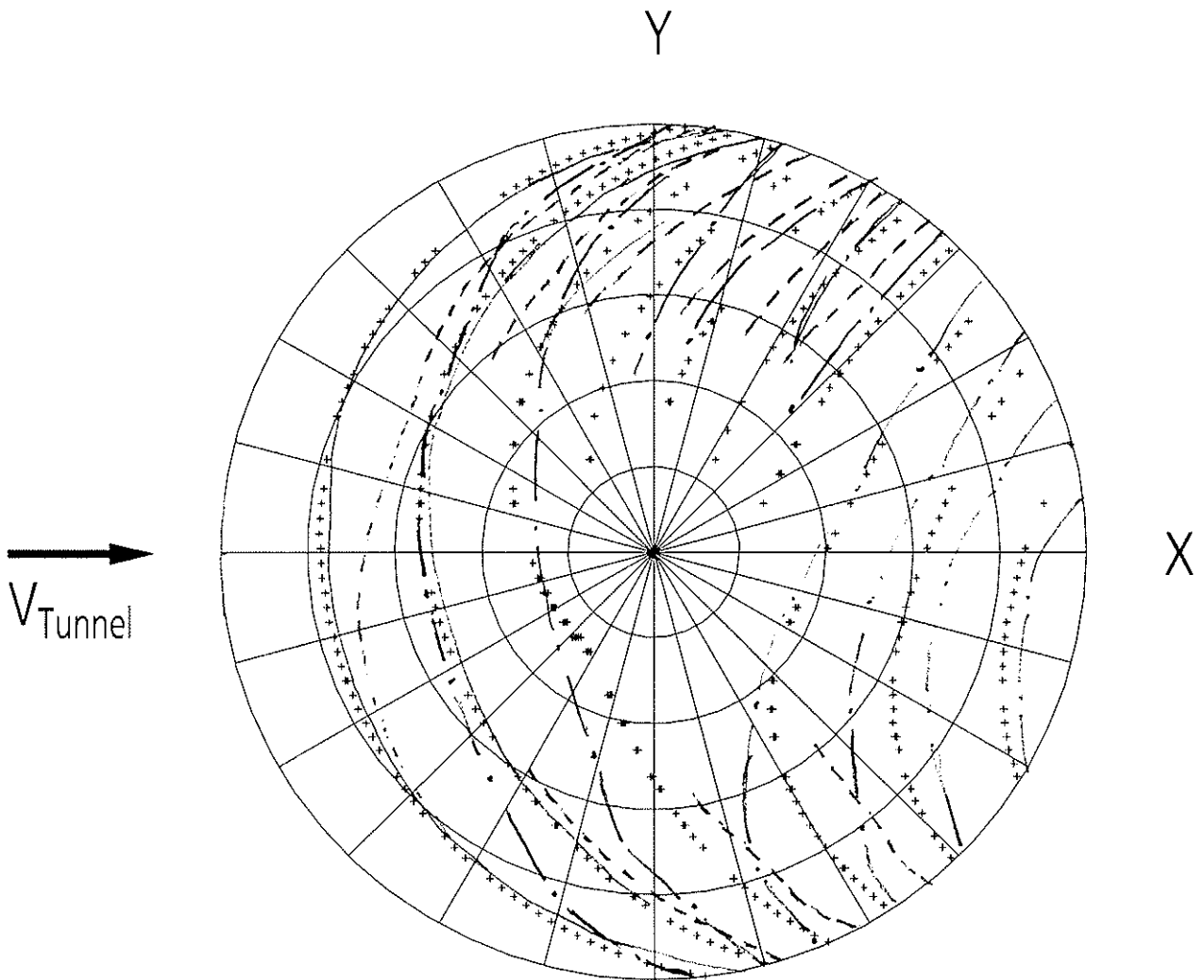
Figure 3: Differences of BVI trajectories in the rotor disk.
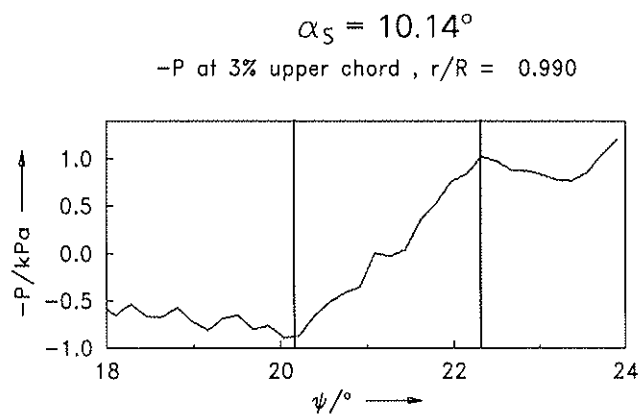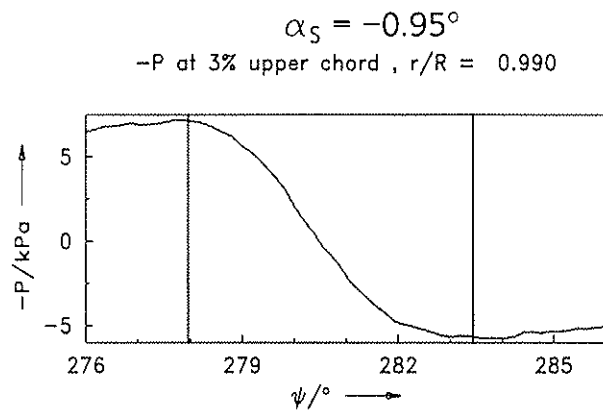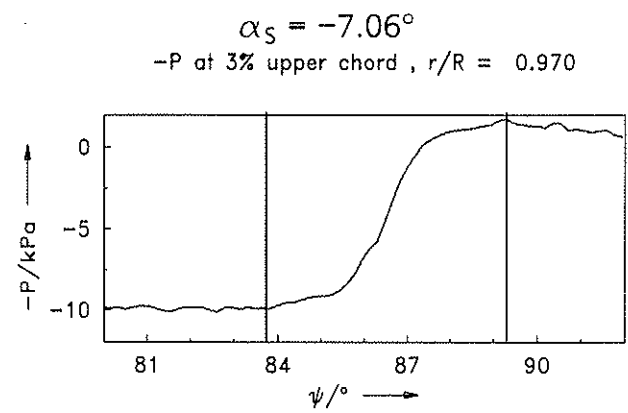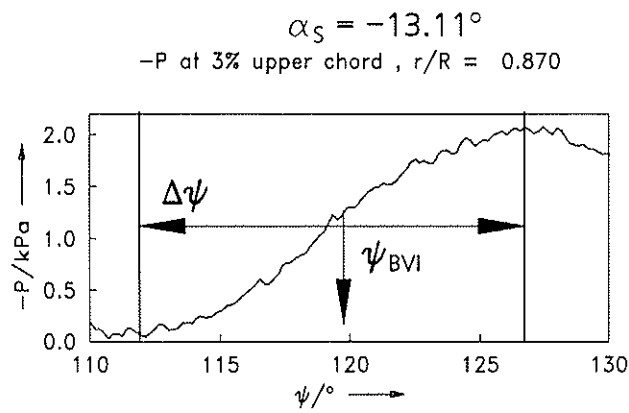
Figure 4: Pressure time histories for vortex core radius analysis.
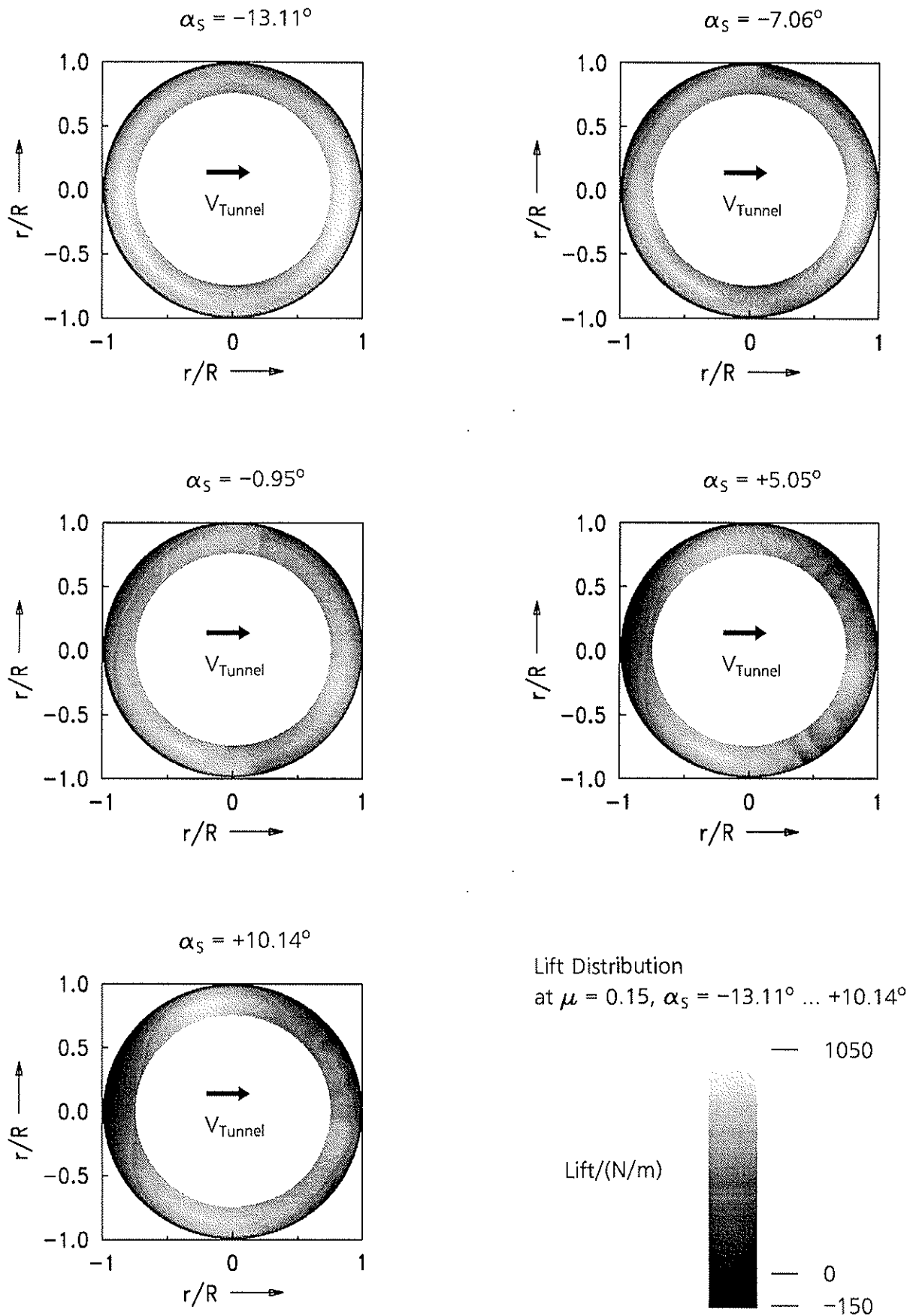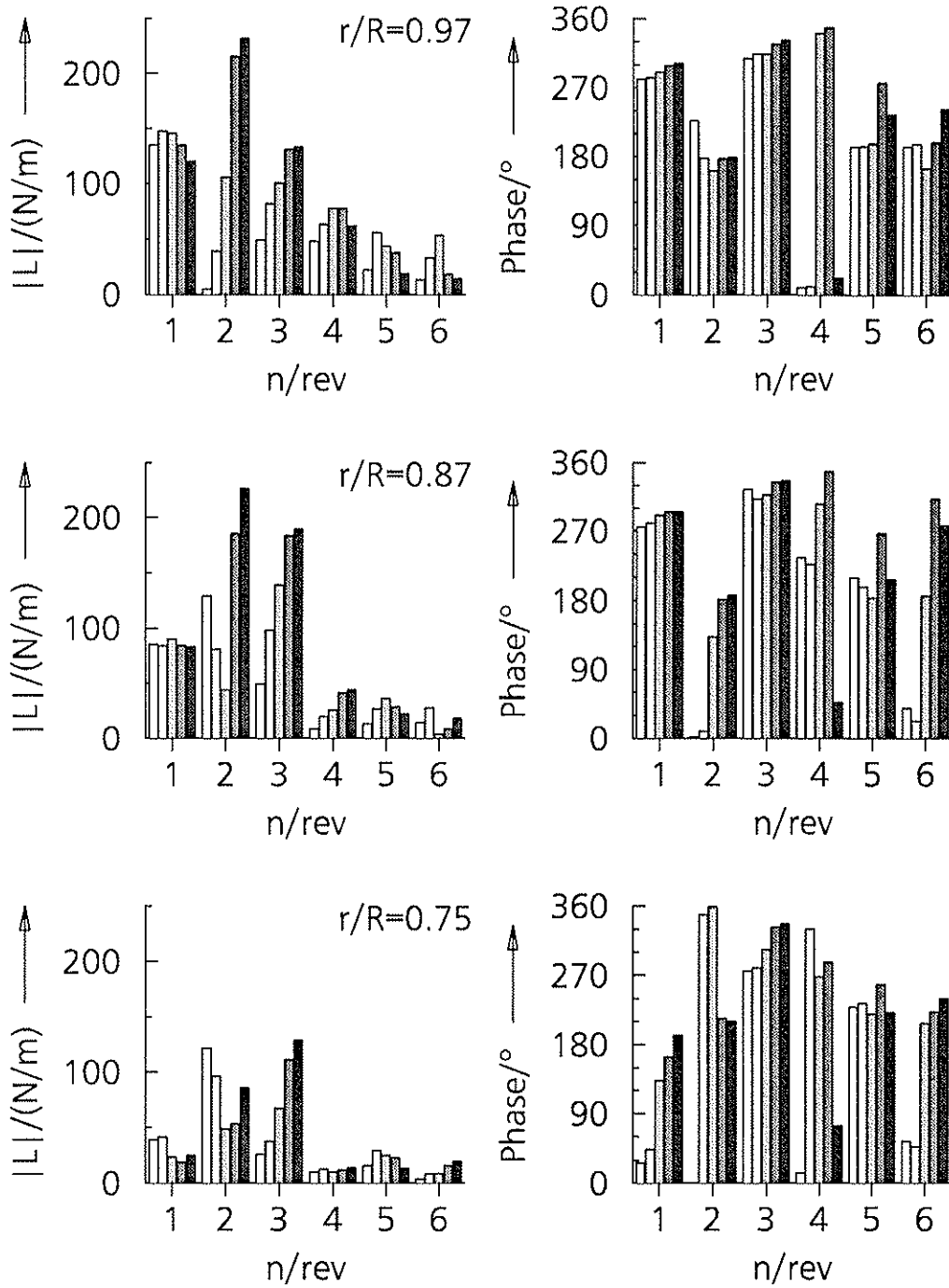
Figure 5: Lift distribution in the rotor disk.

$\alpha_S = -13.11°$

$\alpha_S = -7.06°$

$\alpha_S = -0.95°$

$\alpha_S = +5.05°$

$\alpha_S = +10.14°$

Lift Distribution
at $\mu = 0.15$, $\alpha_S = -13.11° \ldots +10.14°$

1050

Lift/(N/m)

0

−150
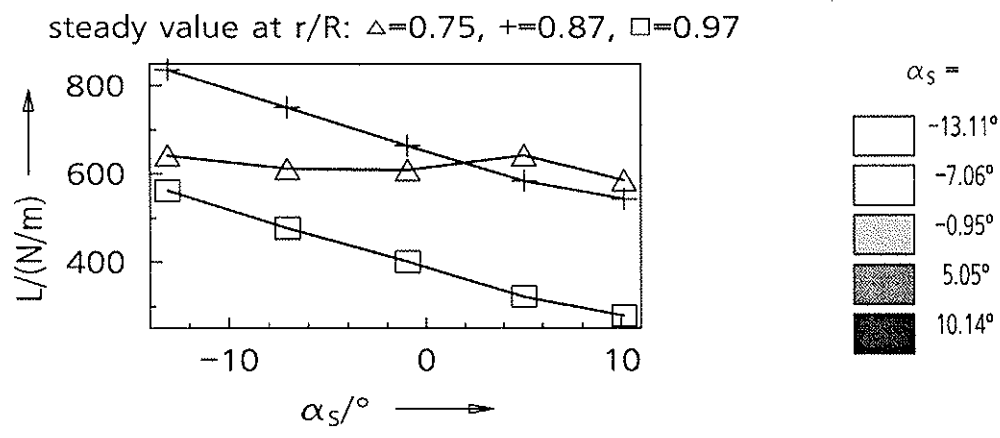
Figure 6: Lift spectra dependency on shaft angle.
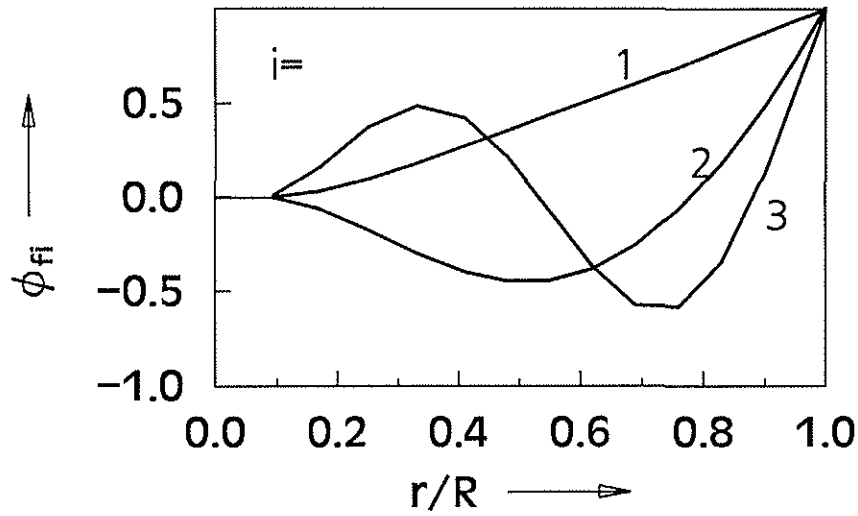
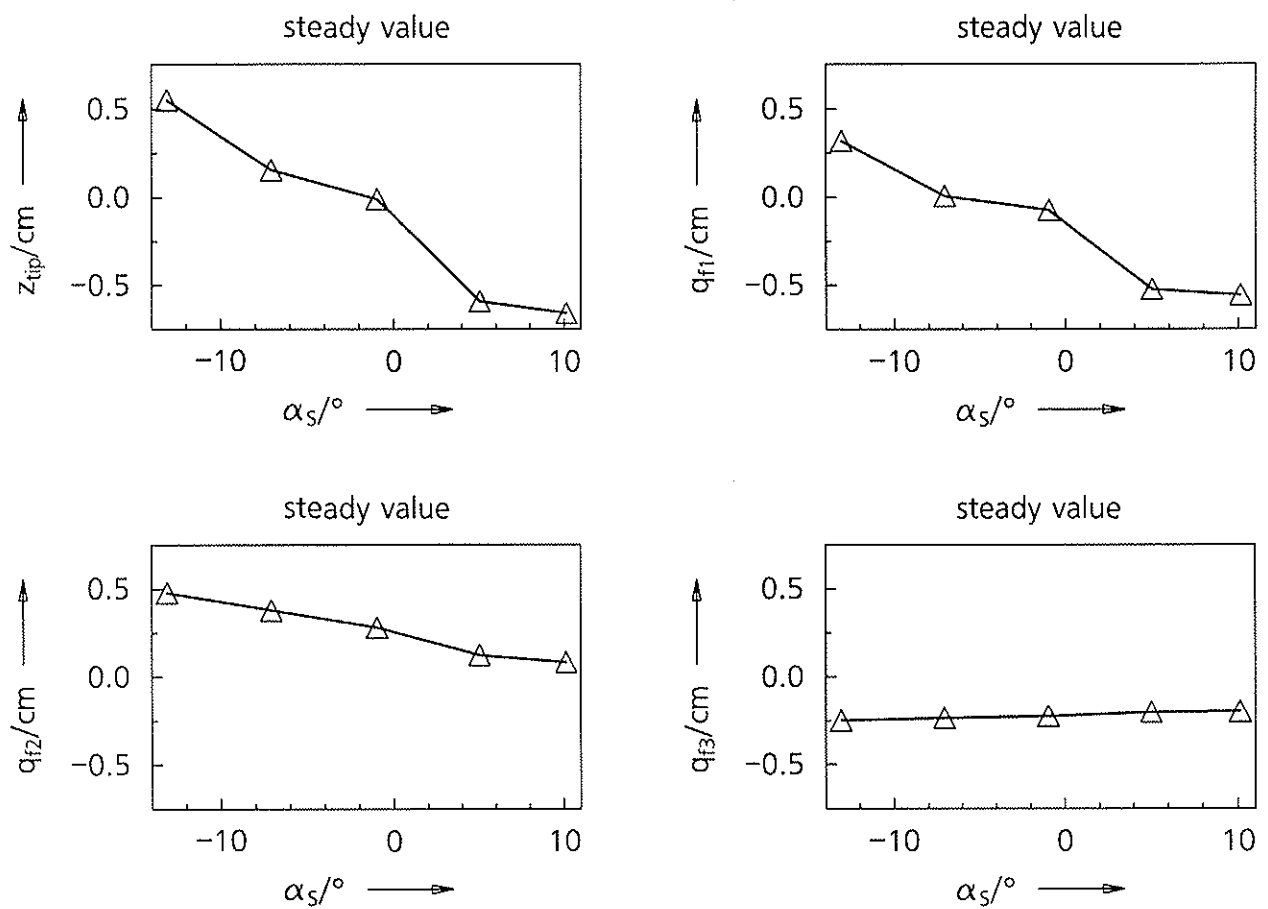Figure 7: First three flap mode shapes of BO105 model rotor.

Figure 8: Dependency of steady tip deflection (measured) and flap mode deflection (identified) on shaft angle.
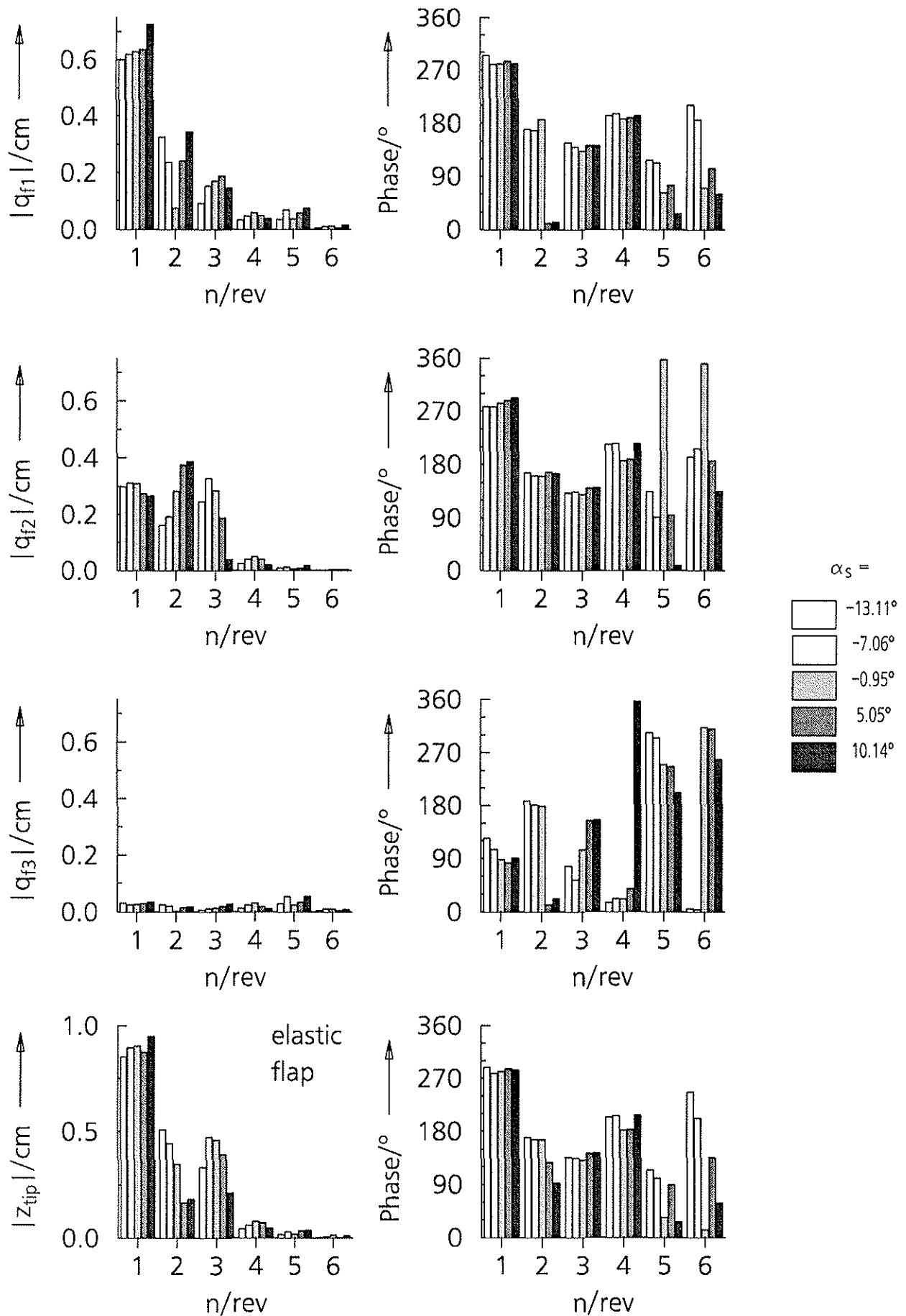
Figure 9: Dependency of dynamic tip deflection (measured) and flap mode deflection (identified) on shaft angle.